

RESEARCH ARTICLE

Quantitative Analysis of Heterogeneous [¹⁸F]FDG Static (SUV) vs. Patlak (Ki) Whole-body PET Imaging Using Different Segmentation Methods: a Simulation Study

Mingzan Zhuang,^{1,2} Nicolas A. Karakatsanis,^{3,4} Rudi A. J. O. Dierckx,¹ Habib Zaidi^{1,5,6,7}

¹Department of Nuclear Medicine and Molecular Imaging, University of Groningen, 9700 RB, Groningen, Groningen, Netherlands

²The Key Laboratory of Digital Signal and Image Processing of Guangdong Province, Shantou University, Shantou, China

³Division of Radiopharmaceutical Sciences, Department of Radiology, Weill Cornell Medical College, Cornell University, New York, NY, 10021, USA

⁴Translational and Molecular Imaging Institute, Icahn School of Medicine at Mount Sinai, New York, NY, 10029, USA

⁵Division of Nuclear Medicine and Molecular Imaging, Geneva University Hospital, 1211, Geneva, Switzerland

⁶Geneva University Neurocenter, University of Geneva, 1205, Geneva, Switzerland

⁷Department of Nuclear Medicine, University of Southern Denmark, 5000, Odense, Denmark

Abstract

Purpose: Whole-body (WB) dynamic positron emission tomography (PET) enables imaging of highly quantitative physiological uptake parameters beyond the standardized uptake value (SUV). We present a novel dynamic WB anthropomorphic PET simulation framework to assess the potential of 2-deoxy-2-[¹⁸F]fluoro-D-glucose ([¹⁸F]FDG) net uptake rate constant (Ki) imaging in characterizing tumor heterogeneity.

Procedures: Validated heterogeneous [¹⁸F]FDG tumor kinetics were modeled within the XCAT phantom (ground truth). Thereafter, static (SUV) and dynamic PET data were simulated and reconstructed, followed by indirect WB Patlak Ki imaging. Subsequently, we compared the methods of affinity propagation (AP) and automatic segmentation with active contour (MASAC) to evaluate the impact of tumor delineation. Finally, we extracted the metabolically active tumor volume (MATV), Dice similarity coefficient (DSC), and the intratumoral heterogeneity metrics of the area under the cumulative intensity histogram curve (CIH_{AUC}), homogeneity, entropy, dissimilarity, high-intensity emphasis (HIE), and zone percentage (ZP), along with the target-to-background (TBR) and contrast-to-noise ratios (CNR).

Results: Ki images presented higher TBR but lower CNR compared to SUV. In contrast to MASAC, AP segmentation resulted in smaller bias for MATV and DSC scores in Ki compared to SUV images. All metrics, except for ZP, were significantly different in AP segmentation between SUV and Ki images, with significant correlation observed for MATV, homogeneity, dissimilarity, and entropy. With MASAC segmentation, CIH_{AUC} , homogeneity, and dissimilarity were significantly different between SUV and Ki images, with all metrics, except for HIE and ZP, being significantly correlated. In ground truth images, increased heterogeneity was observed

with Ki compared to SUV, with a high correlation for all metrics.

Conclusions: A novel simulation framework was developed for the assessment of the quantitative benefits of WB Patlak PET on realistic heterogeneous tumor models. Quantitative analysis showed that WB Ki imaging may provide enhanced TBR and facilitate lesion segmentation and quantification beyond the SUV capabilities.

Key words: PET, Whole-body, Parametric imaging, Segmentation, Heterogeneity

Introduction

Positron emission tomography (PET) imaging employing 2-deoxy-2-[¹⁸F]fluoro-D-glucose ([¹⁸F]FDG) is commonly used in clinical oncology for diagnosis, staging, restaging, radiation therapy treatment planning, and the assessment of treatment outcome [1–3]. Beyond the currently established static PET imaging protocols, the analysis of dynamic PET data might also enable the extraction of highly reproducible kinetic features of the [¹⁸F]FDG uptake for in-depth and quantitative characterization of tumor glucose metabolism over the course of treatment. Several investigators have demonstrated the feasibility of utilizing dynamic PET imaging in the clinic for the objective characterization of a spectrum of kinetic metabolic parameters in oncologic malignancies [4, 5]. However, these techniques were restricted to single bed positions, thus preventing their application to whole-body (WB) imaging to quantify primary and metastatic malignancies across multiple tissues in the same exam [6]. Recently, WB dynamic [¹⁸F]FDG PET imaging protocols have started gaining interest in clinical oncology owing to their ability to deliver highly quantitative parametric WB PET images, beyond the conventional standardized uptake value (SUV) metric, by tracking both the spatial and temporal distributions of the [¹⁸F]FDG uptake over multiple bed positions [7].

In the meantime, a number of intratumoral uptake heterogeneity metrics in [¹⁸F]FDG PET have recently been shown to correlate with treatment response [8, 9]. The use of these metrics can be extended to parametric imaging, where they may exhibit different effects compared to SUV images that can be clinically useful. Previous studies reported significant differences in the metabolically active tumor volume (MATV) scores between SUV and parametric images [10, 11]. Tixier et al. [9] assessed a number of metrics linked to tumor uptake heterogeneity in non-small cell lung cancer and reported high correlations for all metrics between SUV and parametric images. However, the lack of ground truth (GT) in clinical studies made it difficult to draw further conclusions. Therefore, the systematic comparison of the performance of a range of oncologic image-derived PET metrics between SUV and parametric images, where the GT is known *a priori*, is highly desirable.

The purpose of the present work is to develop a novel WB dynamic anthropomorphic [¹⁸F]FDG PET simulation framework supporting realistic tumor heterogeneity models

to assess the performance of a wide spectrum of advanced PET image metrics in WB Patlak-derived uptake rate constant (Ki) imaging, with respect to SUV. In addition, two automated segmentation algorithms were employed to assess the impact of tumor delineation on the extracted features.

Materials and Methods

Dynamic Anthropomorphic Phantom Simulation

To perform realistic simulations, we constructed dynamic WB PET anthropomorphic emission and attenuation maps from the extended cardio-torso (XCAT) phantom along with a respiratory motion model [12]. In addition, we modeled a heterogeneous set of [¹⁸F]FDG time-activity curves (TACs) for a range of tissues (Fig. 1) using a validated two-tissue compartment model and a set of [¹⁸F]FDG kinetic parameter values reported in the literature (Table 1). Subsequently, each of the generated TACs was assigned to its corresponding tissue region in the XCAT phantom.

According to a previously proposed clinical WB dynamic PET acquisition protocol [18], we first considered a dynamic PET acquisition (1st phase) centered over the heart corresponding to the first 6 min post-injection (p.i.) of [¹⁸F]FDG, including 12 × 10 s and 12 × 20 s frames. This is followed by simulation of six unidirectional (head-to-thighs) WB passes (2nd phase) consisting of seven bed positions, each scanned for 45 s. An input function model reported by Feng et al. [19] was adopted in our simulations, sampled at the mid-time points of the first 24 cardiac frames of the first phase and the six subsequent cardiac frames of the second phase.

Subsequently, realistic tumor shapes with three different levels of [¹⁸F]FDG uptake were modeled and incorporated within the extended cardiac-torso (XCAT) phantom according to a technique proposed by Le Maitre et al. to reflect the intratumoral uptake heterogeneity typically observed in clinical oncologic PET studies [20]. Specifically, different irregularly shaped heterogeneities were segmented using an adaptive thresholding technique within a set of modeled tumors (7 lung tumors and 6 cases with laryngeal squamous cell carcinoma from Louvain database) [21, 22]. The low-activity region of the tumor, which we assume contains both high and middle activity concentration levels, was segmented using a thresholding value of 0.5 (T_{Low}) on normalized images on [0–1] scale. Then, the value at the

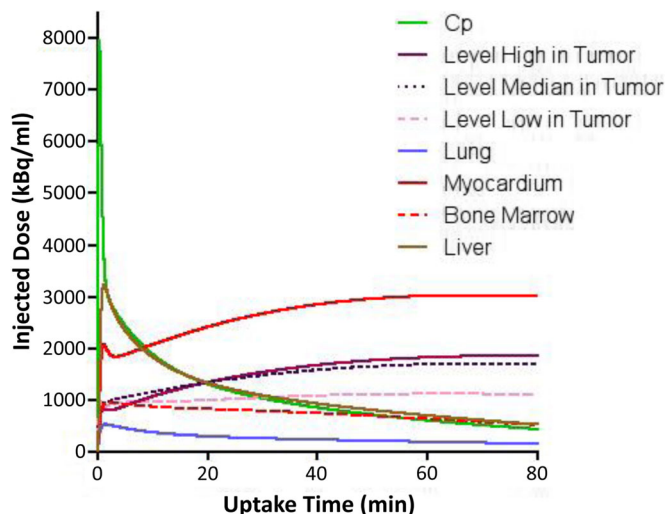


Fig. 1. Noise-free TACs for different tissues derived from the kinetic parameters shown in Table 1 for a 2-compartment kinetic model.

center of the tumor (T_{High}) was used as a threshold to segment the high-activity region within the tumor and the middle value ($(T_{\text{Low}} + T_{\text{High}})/2$) was used as a threshold to segment the middle-activity region for the tumor. Finally, the 3D mesh of these segmented contours was reconstructed using Amide software [23] and converted into three non-uniform rational B-spline (NURBS) surfaces using Rhinoceros software (CADLINK, France), where each surface represented a specific activity level.

We adopted a normal respiratory breathing cycle of 5 s in our simulation and divided it into 10 bins, each representing one of the phases of the periodic respiratory cycle. Then, we utilized the respiratory motion modeling tools of the XCAT phantom to produce for each dynamic PET frame (a given bed position and given pass) 10 respective pairs of emission and attenuation maps, with each pair reflecting the unique anatomy of the tissues at a specific respiration phase. A common respiratory periodic motion pattern was used with a maximum diaphragm motion of 1.5 cm, a maximum anterior-posterior expansion of 0.5 cm, and a normal respiratory cycle of 5 s, as typically observed in our clinical studies. Each emission map was built by assigning the average [^{18}F]FDG activity concentration value for the respective time window of that bed frame, assuming negligible changes in the TACs within the scanning period

(45 s) of a given bed frame during each WB pass (Fig. 1). Subsequently, the above 10 emission maps at each dynamic frame were averaged to produce a single emission map for that frame to model the effects of respiratory motion in our simulated dynamic PET data. Ultimately, a noise-free realistic dynamic emission XCAT phantom was created by repeating the above steps across all bed positions and passes included in our simulated dynamic WB PET scan protocol. In addition, the 10 attenuation maps at each bed position were also averaged to align the effects of respiratory motion between the simulated emission and attenuation maps.

Thereafter, the PET sinograms for each frame were generated using an analytical fully 3D forward projector reflecting the Siemens Biograph™ mCT PET system's detection geometry. Scatter and random count effects were not included in our simulation as these were deemed to have no or limited impact on the outcome. The attenuation coefficient maps were then applied to the emission sinograms. Subsequently, the attenuated PET data were scaled with a global factor to match the nominal sensitivity of the mCT PET scanner and quantitative levels of Poisson noise were added, equivalent to a 45 s acquisition time per bed.

The noisy projection data were later reconstructed using an ordered subsets expectation maximization (OSEM)

Table 1. [^{18}F]FDG kinetic parameters used in the simulation study derived from the literature [13–17]

Tissue	K_1 (ml/(min*g))	k_2 (l/min)	k_3 (l/min)	k_4 (l/min)	V_B (ml/ml)
Level I in lesion	0.180	0.990	0.190	—	0.036
Level II in lesion	0.150	0.550	0.120	—	0.071
Level III in lesion	0.110	0.400	0.073	—	0.095
Normal lung	0.108	0.735	0.016	0.013	0.017
Normal liver	0.864	0.981	0.005	0.016	—
Myocardium	0.600	1.200	0.100	0.001	—
Normal bone marrow	0.200	0.680	0.050	0.020	0.010

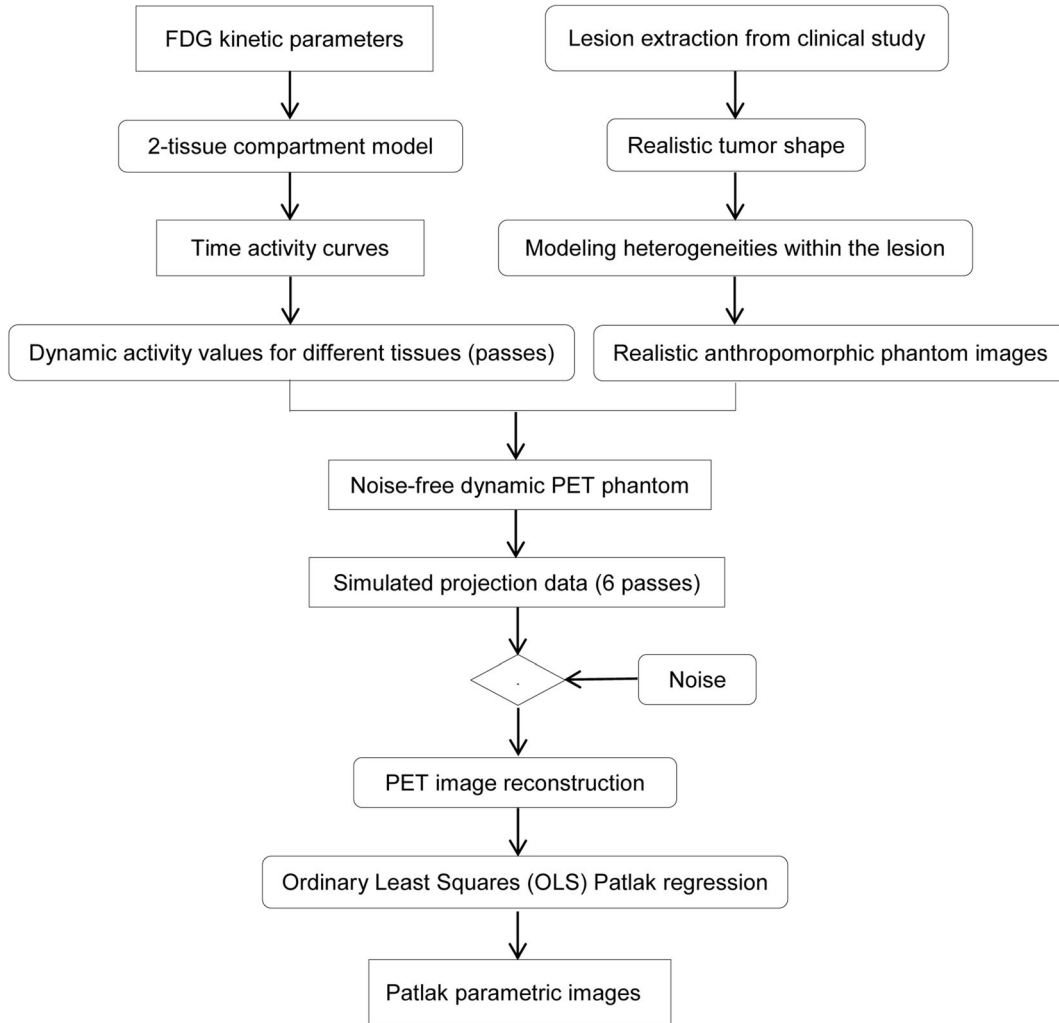


Fig. 2. Flowchart illustrating the various steps involved in the simulation of the realistic dynamic anthropomorphic multi-bed model.

algorithm employing 10 subsets and 40 sub-iterations, using the open-source Software for Tomographic Image Reconstruction (STIR) platform [24]. The matrix size of the image data was 200×200 with a pixel size of $0.50 \times 0.41 \times 0.41 \text{ cm}^3$. The Patlak ordinary least squares (OLS) regression was then applied on the dynamic PET images to estimate K_i images representing the tracer influx rate constant K_i macro-parameter [25]. The flowchart illustrating the above four steps of our simulation framework is shown in Fig. 2. Furthermore, conventional static SUV PET images were generated from a simulated PET dataset involving a single WB pass at 70 min p.i. and lasting 180 s at each bed position.

In total, 13 different lesions (volume range $6.64\text{--}69.34 \text{ cm}^3$) were simulated in the lungs followed by application of a Gaussian smoothing filter of 2 mm on an image matrix of 200×200 voxels for both SUV and K_i images. The GT in SUV images was defined as the noise-free static XCAT images at 70 min p.i. The respective GT in K_i images was obtained after conducting Patlak OLS

regression across six noise-free dynamic XCAT images at different time points.

PET Image Segmentation Algorithms

As reported in earlier studies [26] and more recently in the American Association of Physicists in Medicine (AAPM) Report No. 211, a high variability is observed between different segmentation methods [27]. To assess the impact of tumor delineation, two different segmentation methods, namely a method for automatic segmentation using an active contour model (MASAC) [28] and an affinity propagation algorithm (AP) [29], were employed. These algorithms underwent extensive testing in our lab and were chosen owing to their accuracy and consistency as reported in previous studies using phantom and clinical studies. In particular, the parameter lambda in the implementation of MASAC was set to 3 [28] whereas the default parameters

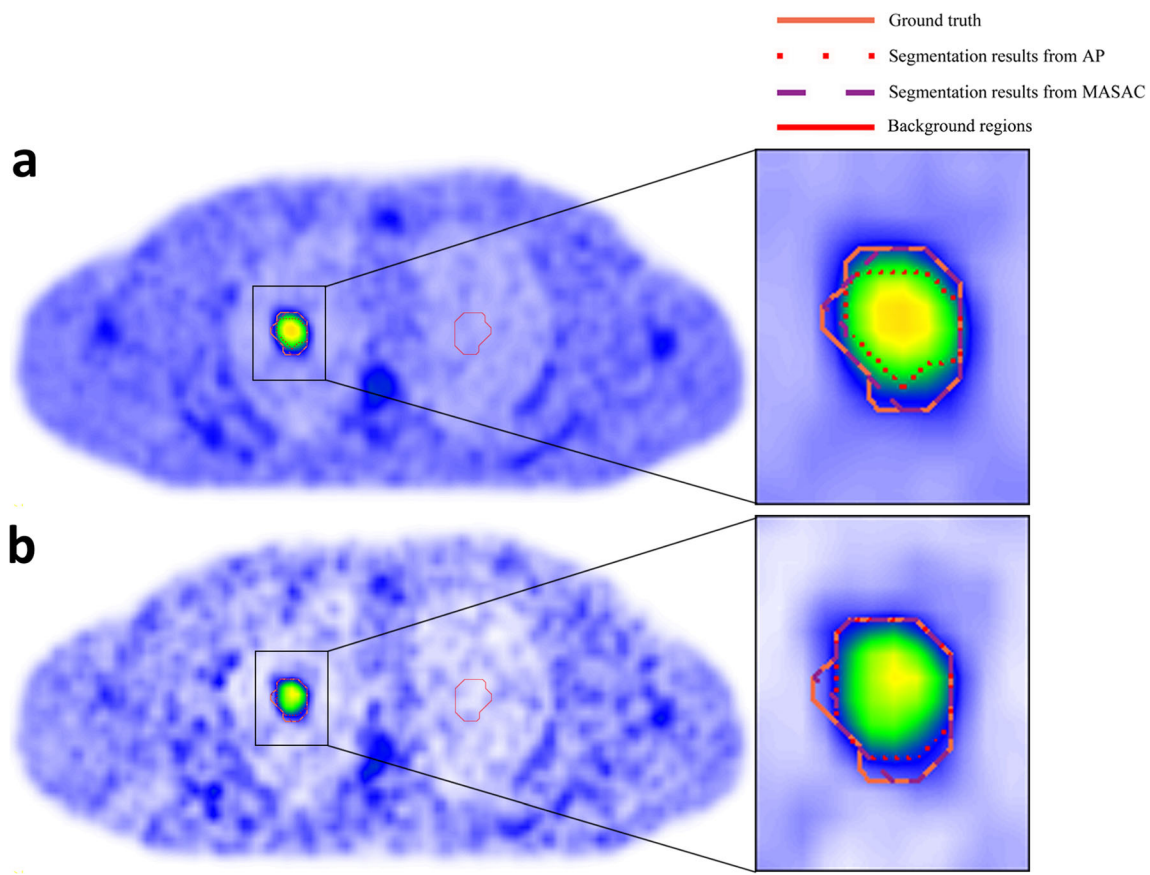


Fig. 3. Representative segmentation results of a realistic anthropomorphic phantom study showing contours by the ground truth (continuous line, orange), AP (dotted line, red) and MASAC (dashed line, purple) on **a** SUV and **b** Ki images. The background regions (continuous line, red) are also indicated.

were used for AP with the largest regional intensity grouping as the segmentation result.

Evaluation Metrics

The MATV, Dice similarity coefficient (DSC), and several intratumoral heterogeneity features were included for the comparison of SUV and Ki images. The DSC was used to assess the accuracy of the geographical match/mismatch

between the segmented volumes and the GT [30, 31], whereas the heterogeneity features were selected because of their reproducibility and robustness as reported in previous studies [8, 9]. Specifically, the area under the cumulative intensity histogram curve (CIH_{AUC}) was considered as a global heterogeneity indicator (with low values indicating a higher degree of heterogeneity), whereas the homogeneity, entropy, dissimilarity, high-intensity emphasis (HIE), and zone percentage (ZP) were chosen as the local heterogeneity-related features. The local heterogeneity

Table 2. Effect size and *P* values resulting from the comparison of the metrics derived between SUV and Ki images

Metric	GT		AP		MASAC	
	Effect size	<i>P</i> value	Effect size	<i>P</i> value	Effect size	<i>P</i> value
MATV	—	—	—0.457	0.001	—0.058	0.937
DSC	—	—	—2.366	0.001	0.074	0.552
CIH_{AUC}	0.597	0.001	4.242	0.001	0.858	0.001
Homogeneity	0.135	0.003	—0.787	0.003	—0.706	0.002
Dissimilarity	0.012	0.701	1.058	0.001	0.991	0.001
Entropy	—0.311	0.001	—0.619	0.001	—0.066	0.701
HIE	0.461	0.004	1.881	0.002	0.567	0.087
ZP	—0.184	0.003	0.232	0.650	0.415	0.136

GT ground truth, MATV metabolically active tumor volume, DSC Dice similarity coefficient, CIH_{AUC} area under the cumulative intensity histogram curve, HIE high-intensity emphasis, ZP zone percentage. Results with $P < 0.05$ are shown in italic

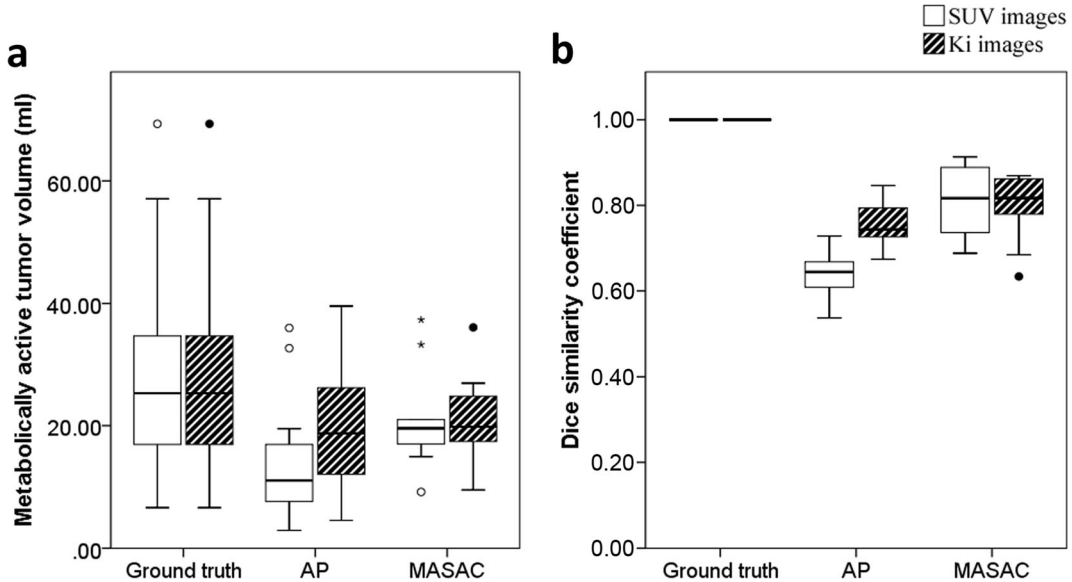


Fig. 4. Box-and-whisker plots comparing segmentation results for **a** metabolically active tumor volumes and **b** Dice similarity coefficient across the simulation studies for SUV and Ki images.

features defined below were derived using *Pyradiomics* software package [32].

$$\text{Homogeneity} = \sum_{i=1}^{Ng} \sum_{j=1}^{Ng} \frac{p(i,j)}{1 + |i-j|} \quad (1)$$

$$\text{Entropy} = - \sum_{i=1}^{Ng} \sum_{j=1}^{Ng} p(i,j) \log_2 p(i,j) \quad (2)$$

$$\text{Dissimilarity} = \sum_{i=1}^{Ng} \sum_{j=1}^{Ng} |i-j| p(i,j) \quad (3)$$

where Ng is the number of gray level intensities and $p(i,j)$ is the (i,j) element in the normalized gray level co-occurrence matrix, representing the number of times for the combination of levels i and j to occur in two pixels in the image, separated by a distance of δ pixels in direction α . In our study, Ng is set to 64 gray levels and δ is 1 over all 13 spatial directions (26-connectivity in 3D).

$$\text{HIE} = \frac{\sum_{i=1}^{Ng} \sum_{j=1}^{Ns} P(i,j) i^2}{\sum_{i=1}^{Ng} \sum_{j=1}^{Ns} P(i,j)} \quad (4)$$

$$\text{ZP} = \sum_{i=1}^{Ng} \sum_{j=1}^{Ns} \frac{P(i,j)}{Np} \quad (5)$$

where Ng is the number of gray level intensities in the gray level size zone matrix, Ns is the number of discrete zone sizes, Np is the number of voxels, and $P(i,j)$ represents the

number of one or more connected gray level zones that share the gray level i and size j in the image.

Additionally, the target-to-background ratio (TBR) and contrast-to-noise ratio (CNR) were employed to assess the contrast and noise in SUV and Ki images, as defined below:

$$TBR = \frac{Mean_T}{Mean_B} \quad (6)$$

$$CNR = \frac{Mean_T - Mean_B}{Std_B} \quad (7)$$

where $Mean_T$ and $Mean_B$ are the mean values for the tumor (target) and background regions, respectively, and Std_B is the standard deviation of the background region.

Statistical Analysis

Statistical analysis was conducted using the SPSS 24.0 commercial software package (IBM, Chicago, USA). A non-parametric Wilcoxon test was used to assess if the differences between each pair of methods compared in this study were significant or not, with a P value of 0.05 denoting significance. The correlation of various evaluated metrics between SUV and Ki images was assessed using the non-parametric Spearman analysis, with a P value of 0.05 determining statistical significance. Statistical analysis results were presented using box-and-whisker plots, providing lower to upper quartiles (25th to 75th percentile, central box), the median (middle line of the box), and the outliers, as identified in Tukey's method ($1.5 \times$ inter-quartile range) [33]. In addition, scatter plots were also used to explore the relationships between different groups of data.

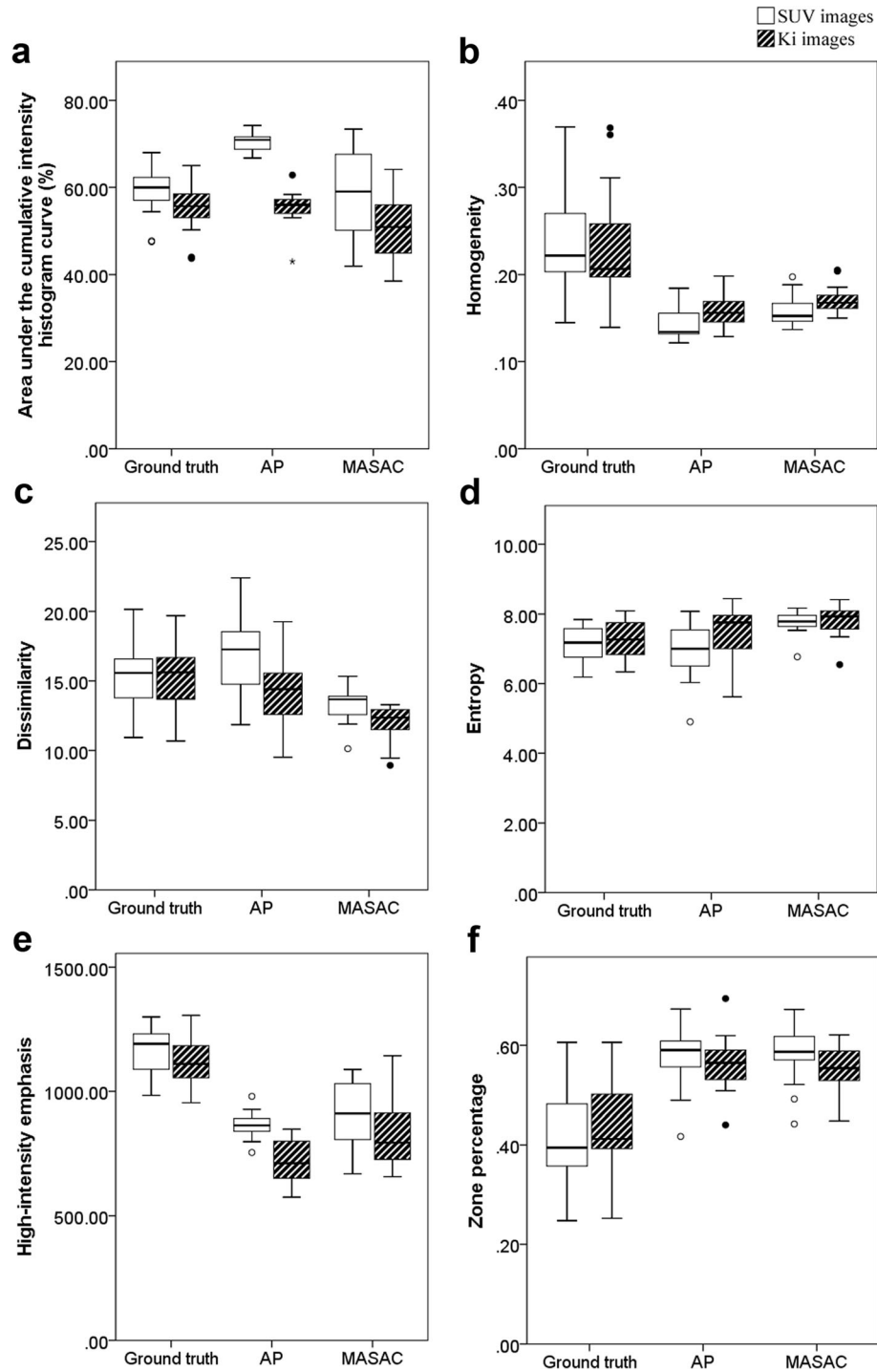


Fig. 5. Box-and-whisker plots comparing the heterogeneity metrics: **a** area under the cumulative intensity histogram curve, **b** homogeneity, **c** dissimilarity, **d** entropy, **e** high-intensity emphasis, and **f** zone percentage across the simulation studies for SUV and Ki images.

Results

SUV vs. Ki Image Segmentation

The contours extracted by both segmentation methods of a representative realistic anthropomorphic phantom study are

presented in Fig. 3. It can be seen that both segmentation techniques could delineate the tumors properly on either SUV or Ki images. Similar results were also observed in other cases included in this study. The average TBR in Ki images for all lesions (6.25) was significantly enhanced compared to that (4.77) in SUV images ($P < 0.002$), whereas

Table 3. Correlation coefficient and P values resulting from the correlations analysis of the metrics derived using the different segmentation methods between SUV and Ki images. (Abbreviations as in Table 2. Results with $P < 0.05$ are shown in italic)

Metrics	GT		AP		MASAC	
	Coefficient	P value	Coefficient	P value	Coefficient	P value
MATV		—	0.912	< 0.001	0.847	< 0.001
DSC		—	0.511	0.074	0.753	0.003
CIH _{AUC}	0.973	< 0.001	0.440	0.133	0.890	< 0.001
Homogeneity	0.989	< 0.001	0.670	0.012	0.720	0.006
Dissimilarity	0.995	< 0.001	0.868	< 0.001	0.945	< 0.001
Entropy	0.956	< 0.001	0.901	< 0.001	0.720	0.006
HIE	0.956	< 0.001	-0.137	0.655	0.516	0.071
ZP	0.989	< 0.001	0.154	0.616	0.500	0.082

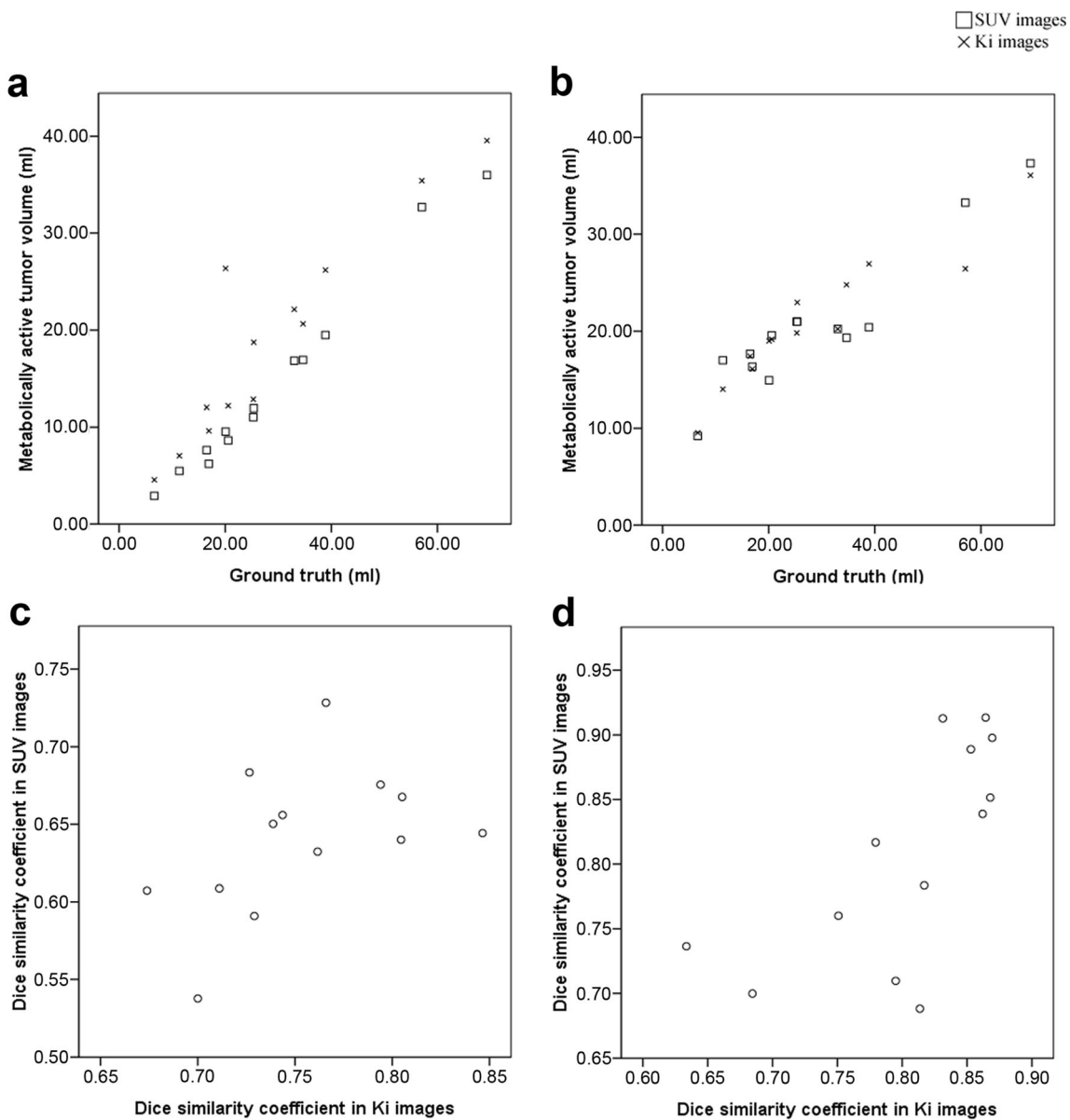


Fig. 6. Scatter plots comparing the segmentation results from AP (a and c) and MASAC (b and d) for metabolically active tumor volume (a and b) and Dice similarity coefficient (c and d) across the simulation studies for SUV and Ki images.

Table 4. Effect size and *P* values resulting from the comparison of the metrics derived between different segmentation methods. (Abbreviations as in Table 2. Results with *P*<0.05 are shown in italic)

Metric	SUV images		Ki images	
	Effect size	<i>P</i> value	Effect size	<i>P</i> value
MATV	-0.712	<i>0.001</i>	-0.216	0.278
DSC	-2.468	<i>0.001</i>	-0.764	0.046
CIH _{AUC}	<i>1.603</i>	<i>0.001</i>	0.790	0.039
Homogeneity	-0.798	<i>0.001</i>	-0.703	<i>0.004</i>
Dissimilarity	<i>1.530</i>	<i>0.001</i>	1.022	<i>0.002</i>
Entropy	-1.283	<i>0.001</i>	-0.517	0.019
HIE	-0.358	0.382	-0.915	0.023
ZP	-0.055	0.753	0.084	0.972

SUV images achieved significantly better average CNR (34.36) over Ki images (13.70, *P*<0.002).

Compared to SUV images, Ki images yielded smaller average bias in MATV (SUV -52.77 %, Ki -31.62 %) and DSC (SUV -36.00 %, Ki -25.00 %) with AP, whereas no significant differences were observed in MATV and DSC for MASAC algorithm (Table 2 and Fig. 4). Except for ZP, most heterogeneity metrics were significantly different between SUV and Ki images for AP segmentation, and a similar trend was also observed for CIH_{AUC}, homogeneity, and dissimilarity with MASAC segmentation (Table 2 and Fig. 5). Besides, a general trend of correlation between SUV and Ki images was observed for MATV, homogeneity, dissimilarity, and entropy with AP segmentation, whereas most metrics were found to be significantly correlated between SUV and Ki images, except for HIE and ZP, when using MASAC segmentation algorithm (Table 3, Fig. 6 and Supplemental Material S1-S2).

SUV vs. Ki Images in Noise-Free GT

Most heterogeneity features, except dissimilarity, exhibited statistically significant differences between SUV and Ki noise-free GT images (Table 2). More specifically, slightly decreased CIH_{AUC} (-6.28 %), homogeneity (-3.99 %), and HIE (-3.95 %) along with increased entropy (2.21 %) and

ZP (4.52 %) were observed in Ki noise-free GT images compared with SUV GT images (Fig. 5). Besides, it could be observed from Table 3 that all heterogeneity features were highly correlated between SUV and Ki noise-free GT images (*P*<0.001).

AP vs. MASAC Segmentation

There is no significant difference in the MATV metric between the two segmentation algorithms for Ki images (Table 4). MASAC yielded smaller bias in DSC (-20.00 %) for Ki images and smaller bias in MATV (-33.75 %) and DSC (-19.00 %) for SUV images, compared to AP.

Segmentation Results vs. Noise-Free GT

Compared to noise-free GT images, most metrics derived from segmentation results, except CIH_{AUC} and entropy in some cases, were significantly different in either SUV or Ki images (Table 5). In addition, both MASAC and AP presented lower MATV, homogeneity, and HIE, and higher ZP scores for SUV and Ki images compared to GT (Figs. 4 and 5).

Discussion

A clinically feasible WB dynamic PET acquisition protocol enabling highly quantitative multi-parametric PET imaging across multiple bed positions was presented in previous studies [7, 34]. In this work, we developed a multi-bed dynamic 4D XCAT-based realistic simulation framework supporting tumor heterogeneity modeling, to be utilized for (i) evaluation of WB 4D PET image reconstruction and segmentation algorithms, (ii) optimization of dynamic WB PET acquisition and image analysis methods, (iii) modeling of the WB pharmacokinetic properties of novel drugs under development, and (iv) assessment of the usefulness of a wide range of quantitative metrics in Ki vs. SUV images. Moreover, our framework allowed the extraction of useful conclusions by enabling the assessment of a wide range of

Table 5. Effect size and *P* values resulting from the comparison of the derived metrics compared with the ground truth. (Abbreviations as in Table 2. Results with *P*<0.05 are shown in italic)

	AP vs. GT				MASAC vs. GT			
	SUV images		Ki images		SUV images		Ki images	
	Effect size	<i>P</i> value	Effect size	<i>P</i> value	Effect size	<i>P</i> value	Effect size	<i>P</i> value
MATV	-1.006	<i>0.001</i>	-0.668	<i>0.004</i>	-0.610	<i>0.033</i>	-0.587	<i>0.033</i>
DSC	-	-	-	-	-	-	-	-
CIH _{AUC}	<i>2.662</i>	<i>0.001</i>	0.063	0.753	-0.040	0.701	-0.667	<i>0.019</i>
Homogeneity	-1.933	<i>0.001</i>	-1.472	<i>0.002</i>	-1.652	<i>0.002</i>	-1.236	<i>0.005</i>
Dissimilarity	<i>0.605</i>	<i>0.001</i>	-0.480	<i>0.009</i>	-0.915	<i>0.002</i>	-1.617	<i>0.001</i>
Entropy	-0.326	0.279	0.202	0.753	1.454	<i>0.002</i>	0.982	<i>0.005</i>
HIE	-3.698	<i>0.001</i>	-4.196	<i>0.001</i>	-1.998	<i>0.001</i>	-2.522	<i>0.001</i>
ZP	<i>1.719</i>	<i>0.001</i>	1.343	<i>0.002</i>	1.816	<i>0.002</i>	1.345	<i>0.005</i>

metrics under noise-free conditions. In particular, the Ki noise-free GT images showed increased heterogeneity, in terms of lower CIH_{AUC}, homogeneity, and HIE, and higher entropy and ZP, compared to SUV GT images, thereby indicating that heterogeneity features can be different between SUV and Ki images. Independent of the PET segmentation algorithm and the type of images analyzed (SUV vs. Ki), a lower homogeneity, a lower HIE, and a higher ZP were observed on simulated noisy against noise-free GT images. This is attributed to the relatively higher degree of heterogeneity expected for noisy PET images.

Furthermore, our findings indicate that WB Ki imaging can provide enhanced TBR as well as an additional set of highly quantitative tumor features, beyond the static features currently supported with the respective SUV image metrics (Fig. 3). Our results are consistent with observations made in previous studies. In particular, Chen et al. [35] reported that gradient-based tumor delineation method may be more accurate on Patlak Ki parametric maps compared to conventional static SUV images using magnetic resonance imaging as the GT. Furthermore, Llan et al. [36] found that Ki images present better tumor-to-liver contrast compared with SUV images. Finally, Wangerin et al. [37] assessed the variations during the PET imaging process using a series of linked simulations and found that Ki images were associated with superior receiver operating characteristic performance compared to SUV images.

In our study, significant correlations were also found between SUV and Ki images, regardless of the segmentation method. It should be noted that parametric Ki images may still be complementary to SUV even when a high correlation is observed between the two images, as they are essentially different quantities, each providing information that cannot be deduced from the other. This is because Ki imaging measures the tracer net uptake rate during a relatively long scan time window post-injection, whereas SUV imaging measures the average absolute uptake of the tracer within a relatively short scan time window post-injection. However, a systematic evaluation of the clinical usefulness of the added information derived from WB Ki imaging is beyond the scope of the current work. We are planning to utilize the findings of this study to evaluate the same metrics using a large clinical database acquired with a recently proposed combined SUV/Patlak imaging framework [38, 39].

We have also observed that the MATV was systematically underestimated on both SUV and Ki images regardless of the segmentation algorithm. It should be noted that the presence of respiratory motion is expected to have amplified the actual MATV due to motion blurring. Therefore, for routine clinical operation, respiratory motion and its varying effect on SUV and Ki metrics should be carefully considered.

A number of practical limitations are associated with this study. Firstly, the potential efficiency variance across all PET detector pairs was not modeled. We also assumed no scatter and random effects in our analytic simulations.

Furthermore, a regular periodic respiratory motion pattern was adopted. Patient's irregular free breathing would have caused asymmetric blurring of focal lesions, thereby resulting in less predictable artifacts. Moreover, the number of evaluated cases in this study may not be sufficient. Nevertheless, we aim at a systematic follow-up study using a larger sample to investigate the effect of different acquisition/reconstruction protocols on various clinical PET scanners, across a typical range of lesion sizes and contrasts observed in clinical studies. In addition, the time-averaging of attenuation maps in our study is adopted to simplify the simulation, which may not reflect the actual process of attenuation as the measurement model in the attenuation map is non-linear. Finally, in the absence of guidelines on optimal reconstruction parameters for parametric Ki images, both Ki and SUV images have been reconstructed using the same iteration numbers. Further investigations of optimal reconstruction protocols for parametric imaging are warranted.

Conclusion

A dynamic multi-bed PET simulation framework was developed based on the 4D XCAT anthropomorphic model, respiratory motion and tumor heterogeneity models, and validated ¹⁸F-FDG kinetic parameters to enable the systematic evaluation of the clinical usefulness of WB parametric PET imaging for various types of oncologic malignancies beyond the currently established SUV metric. Our results showed that Ki images may provide enhanced TBR and further facilitate lesion segmentation and quantification beyond the SUV capabilities, thereby demonstrating the potential of hybrid SUV/Ki imaging, in terms of lesion quantification.

Funding Information. This work was supported by the Swiss National Science Foundation under grant SNSF 3200030_176052, the Swiss Cancer Research Foundation under Grant KFS-3855-02-2016, and an Open Grant (2014GDDSIPL-06) from the Key Laboratory of Digital Signal and Image Processing of Guangdong Province, Shantou University.

Compliance with Ethical Standards

Conflict of Interest

The authors declare that they have no conflict of interest.

References

- Chung MK, Jeong HS, Park SG, Jang JY, Son YI, Choi JY, Hyun SH, Park K, Ahn MJ, Ahn YC, Kim HJ, Ko YH, Baek CH (2009) Metabolic tumor volume of [¹⁸F]-fluorodeoxyglucose positron emission tomography/computed tomography predicts short-term outcome to radiotherapy with or without chemotherapy in pharyngeal cancer. Clin Cancer Res 15:5861–5868
- La TH, Filion EJ, Turnbull BB et al (2009) Metabolic tumor volume predicts for recurrence and death in head-and-neck cancer. Int J Radiat Oncol Biol Phys 74:1335–1341

3. Obara P, Pu YL (2013) Prognostic value of metabolic tumor burden in lung cancer. *Chin J Cancer Res* 25:615–622
4. Kristian A, Revheim ME, Qu H, Mælandsmo GM, Engebråten O, Seierstad T, Malinen E (2013) Dynamic ^{18}F -FDG-PET for monitoring treatment effect following anti-angiogenic therapy in triple-negative breast cancer xenografts. *Acta Oncol* 52:1566–1572
5. Dimitrakopoulou-Strauss A, Pan L, Strauss LG (2012) Quantitative approaches of dynamic FDG-PET and PET/CT studies (dPET/CT) for the evaluation of oncological patients. *Cancer Imaging* 12:283–289
6. Zaidi H, Karakatsanis N (2018) Towards enhanced PET quantification in clinical oncology. *Br J Radiol* 91:20170508
7. Karakatsanis NA, Casey ME, Lodge MA, Rahmim A, Zaidi H (2016) Whole-body direct 4D parametric PET imaging employing nested generalized Patlak expectation-maximization reconstruction. *Phys Med Biol* 61:5456–5485
8. Hatt M, Majdoub M, Vallières M, Tixier F, le Rest CC, Groheux D, Hindie E, Martineau A, Pradier O, Hustinx R, Perdrisot R, Guillevin R, el Naqa I, Visvikis D (2015) ^{18}F -FDG PET uptake characterization through texture analysis: investigating the complementary nature of heterogeneity and functional tumor volume in a multi-cancer site patient cohort. *J Nucl Med* 56:38–44
9. Tixier F, Vriens D, Cheze-Le Rest C et al (2016) Comparison of tumor uptake heterogeneity characterization between static and parametric ^{18}F -FDG PET images in non-small cell lung cancer. *J Nucl Med* 57:1033–1039
10. Visser EP, Philippens ME, Kienhorst L et al (2008) Comparison of tumor volumes derived from glucose metabolic rate maps and SUV maps in dynamic ^{18}F -FDG PET. *J Nucl Med* 49:892–898
11. Cheesbunon P, van Velden FH, Yaqub M et al (2011) Measurement of metabolic tumor volume: static versus dynamic FDG scans. *EJNMMI Res* 1:35
12. Segars WP, Sturgeon G, Mendonca S, Grimes J, Tsui BMW (2010) 4D XCAT phantom for multimodality imaging research. *Med Phys* 37:4902–4915
13. Vriens D, Disselhorst JA, Oyen WJG, de Geus-Oei LF, Visser EP (2012) Quantitative assessment of heterogeneity in tumor metabolism using FDG-PET. *Int J Radiat Oncol Biol Phys* 82:E725–E731
14. Dimitrakopoulou-Strauss A, Georgoulas V, Eisenhut M, Herth F, Koukouraki S, Mäcke HR, Haberkorn U, Strauss LG (2006) Quantitative assessment of SSTR2 expression in patients with non-small cell lung cancer using ^{68}Ga -DOTATOC PET and comparison with ^{18}F -FDG PET. *Eur J Nucl Med Mol Imaging* 33:823–830
15. Choi Y, Hawkins RA, Huang SC, Brunken RC, Hoh CK, Messa C, Nitzsche EU, Phelps ME, Schelbert HR (1994) Evaluation of the effect of glucose-ingestion and kinetic-model configurations of FDG in the normal liver. *J Nucl Med* 35:818–823
16. Lin KP, Huang SC, Choi Y, Brunken RC, Schelbert HR, Phelps ME (1995) Correction of spillover radioactivities for estimation of the blood time-activity curve from the imaged lv chamber in cardiac dynamic FDG PET studies. *Phys Med Biol* 40:629–642
17. Sachpekidis C, Mai EK, Goldschmidt H, Hillengass J, Hose D, Pan L, Haberkorn U, Dimitrakopoulou-Strauss A (2015) ^{18}F -FDG dynamic PET/CT in patients with multiple myeloma patterns of tracer uptake and correlation with bone marrow plasma cell infiltration rate. *Clin Nucl Med* 40:E300–E307
18. Karakatsanis NA, Lodge MA, Tahari AK, Zhou Y, Wahl RL, Rahmim A (2013) Dynamic whole-body PET parametric imaging: I. Concept, acquisition protocol optimization and clinical application. *Phys Med Biol* 58:7391–7418
19. Feng D, Huang SC, Wang X (1993) Models for computer simulation studies of input functions for tracer kinetic modeling with positron emission tomography. *Int J Biomed Comput* 32:95–110
20. Le Maitre A, Segars WP, Marache S et al (2009) Incorporating patient-specific variability in the simulation of realistic whole-body F-18 -FDG distributions for oncology applications. *Proc IEEE* 97:2026–2038
21. Wanet M, Lee JA, Weynand B, de Bast M, Poncelet A, Lacroix V, Coche E, Grégoire V, Geets X (2011) Gradient-based delineation of the primary GTV on FDG-PET in non-small cell lung cancer: a comparison with threshold-based approaches, CT and surgical specimens. *Radiother Oncol* 98:117–125
22. Daisne JF, Duprez T, Weynand B, Lonneux M, Hamoir M, Reyhler H, Grégoire V (2004) Tumor volume in pharyngolaryngeal squamous cell carcinoma: comparison at CT, MR imaging, and FDG PET and validation with surgical specimen. *Radiology* 233:93–100
23. Loening AM, Gambhir SS (2003) AMIDE: a free software tool for multimodality medical image analysis. *Mol Imaging* 2:131–137
24. Thielemans K, Tsoumpas C, Mustafovic S, Beisel T, Aguiar P, Dikaios N, Jacobson MW (2012) STIR: software for tomographic image reconstruction release 2. *Phys Med Biol* 57:867–883
25. Patlak CS, Blasberg RG, Fenstermacher JD (1983) Graphical evaluation of blood-to-brain transfer constants from multiple-time uptake data. *J Cereb Blood Flow Metab* 3:1–7
26. Zaidi H, El Naqa I (2010) PET-guided delineation of radiation therapy treatment volumes: a survey of image segmentation techniques. *Eur J Nucl Med Mol Imaging* 37:2165–2187
27. Hatt M, Lee J, Schmidlein CR et al (2017) Classification and evaluation strategies of auto-segmentation approaches for PET: report of AAPM Task Group No. 211. *Med Phys* 44:e1–e42
28. Zhuang M, Dierckx RA, Zaidi H (2016) Generic and robust method for automatic segmentation of PET images using an active contour model. *Med Phys* 43:4483–4494
29. Foster B, Bagci U, Ziyue X et al (2014) Segmentation of PET images for computer-aided functional quantification of tuberculosis in small animal models. *IEEE Trans Biomed Eng* 61:711–724
30. Zou KH, Warfield SK, Bharatha A, Tempany CMC, Kaus MR, Haker SJ, Wells WM III, Jolesz FA, Kikinis R (2004) Statistical validation of image segmentation quality based on a spatial overlap index—scientific reports. *Acad Radiol* 11:178–189
31. Hatt M, le Rest CC, Descourt P et al (2010) Accurate automatic delineation of heterogeneous functional volumes in positron emission tomography for oncology applications. *Int J Radiat Oncol Biol Phys* 77:301–308
32. van Griethuysen JJM, Fedorov A, Parmar C et al (2017) Computational radiomics system to decode the radiographic phenotype. *Cancer Res* 77:e104–e107
33. Frigge M, Hoaglin DC, Iglewicz B (1989) Some implementations of the boxplot. *Am Stat* 43:50–54
34. Karakatsanis NA, Lodge MA, Zhou Y, Wahl RL, Rahmim A (2013) Dynamic whole-body PET parametric imaging: II. Task-oriented statistical estimation. *Phys Med Biol* 58:7419–7445
35. Chen HW, Jiang JZ, Gao JL, Liu D, Axelsson J, Cui M, Gong NJ, Feng ST, Luo L, Huang B (2014) Tumor volumes measured from static and dynamic F-18-fluoro-2-deoxy-D-glucose positron emission tomography-computed tomography scan: comparison of different methods using magnetic resonance imaging as the criterion standard. *J Comput Assist Tomogr* 38:209–215
36. Ilan E, Sandstrom M, Velikyan I, Sundin A, Eriksson B, Lubberink M (2017) Parametric net influx rate images of ^{68}Ga -DOTATOC and ^{68}Ga -DOTATATE: quantitative accuracy and improved image contrast. *J Nucl Med* 58:744–749
37. Wangerin KA, Mužík M, Peterson LM, Linden HM, Nováková A, Mankoff DA, Kinahan PE (2017) A virtual clinical trial comparing static versus dynamic PET imaging in measuring response to breast cancer therapy. *Phys Med Biol* 62:3639–3655
38. Karakatsanis N, Lodge M, Fahrni G et al (2016) Simultaneous SUV/Patlak-4D whole-body PET: a multi-parametric 4D imaging framework for routine clinical application. *J Nucl Med* 57(Suppl. 2):367
39. Karakatsanis N, Lodge M, Zhou Y et al (2015) Novel multi-parametric SUV/Patlak FDG-PET whole-body imaging framework for routine application to clinical oncology. *J Nucl Med* 56(Suppl. 3):625